

High selective synthesis of CaCO₃ superstructures via ultra-homoporous interfacial crystallizer

Mengyuan Wu ^a, Xiaobin Jiang ^{a,*}, Yingshuang Meng ^a, Yuchao Niu ^a, Zhijie Yuan ^a, Wu Xiao ^a, Xiangcun Li ^a, Xuehua Ruan ^b, Xiaoming Yan ^b, Gaohong He ^{a,b}

^a State Key Laboratory of Fine Chemicals, School of Chemical Engineering, Engineering Laboratory for Petrochemical Energy-efficient Separation Technology of Liaoning Province, Dalian University of Technology, Dalian, Liaoning 116024, China

^b School of Petroleum and Chemical Engineering, Dalian University of Technology at Panjin, Panjin 124221, China

ARTICLE INFO

Keywords:

Biomimetic mineralization
Biomaterials synthesis
CaCO₃ superstructure
Microscale diffusion
Interfacial nucleation
Ultra-homoporous channel

ABSTRACT

Precise regulation of biomimetic mineralization for highly ordered superstructures is one of the perpetual concerns in biomaterial synthesis and crystal engineering. Herein, we propose a ultra-homoporous interfacial crystallizer (UHIC) as a novel interfacial microdevice, which has realized high selective synthesis of CaCO₃ superstructures during Gas-Liquid reactive crystallization process. This UHIC with ultra-uniform mass transfer porous channel and interfacial superhydrophilicity render the droplet ultra-homo nucleation site and coordinatively regulate the interfacial nucleation energy. The highly precise microchannel in UHIC can control the CO₂ gas flow rate and sufficient interfacial Gas-Liquid diffusion of the CaCO₃ pre-nucleation cluster (PNC). By coordinating the PNC diffusion, self-organization and nucleus growth, the proportion of synthesized CaCO₃ crystals with spherical and polyhedral structures both increased to higher than 96.77 %, and the crystal size distribution was very uniform (minimum C.V. =11.7%). Fundamental theory of CaCO₃ synthesis with UHIC as a desire interfacial reactive were then outlined, which can shed light on the high-selective synthesis of the microscale biomaterials.

1. Introduction

Biomineralization is a common phenomenon in nature and of importance in the formation of functional biomaterials [1-3]. In principle, the organism could precisely control the crystal structure, morphology and arrangement from the molecular scale to form complex hierarchical structures [4, 5]. The biomimetic hierarchical nano-/microscale materials have a critical potential applications in drug delivery, bone repair, vascular scaffolding, vascular embolization, automotive anti-collision, etc [6-10]. The complicated morphology of natural biominerl crystal was constructed following the non-classical nucleation theory [11], which suggested that the formation of critical pre-cluster and nanoscale nucleation with morphologic plasticity [12-15].

Calcium carbonate was the preferred and classic materials of biomimetic mineralization research, and there were three existed crystalline polymorphs: calcite, aragonite, and vaterite [16-18]. At present, the calcium carbonate was synthesis by rapid mixing and gas diffusion

reactive crystallization method to simulate biological mineralization process [19, 20]. The concept of pre-nucleation cluster (PNC) pathway, was accepted for most relevant precipitation/reactive crystallization processes occurring in aqueous solutions [11, 21-24]. The reactive crystallization interface with short diffusion path and adjustable interfacial reaction energy is the essential features to ensure the diffusion and self-assembly of PNC, which fundamentally determine the high selective synthesis of CaCO₃ with diverse superstructure

Thus, desire interfacial reactive crystallization platform for biomimetic mineralization research and regulation is urgent to hinder the uncontrollable nucleation, formation of amorphous materials within extremely high supersaturation surroundings. In principle, the properties of the heterogeneous nucleation interface, including roughness, intrinsic hydrophobicity, charge and functional groups, were the key factors to optimize the nucleation and reaction kinetics [5, 25-29]. Superhydrophobic solvent interface was an ideal platform for crystallization design, which helped to regulate the proportion of solvent in the interface, adjust the interaction between the interface and crystalline

* Corresponding author.

E-mail addresses: xbjiang@dlut.edu.cn (X. Jiang), hgaohong@dlut.edu.cn (G. He).

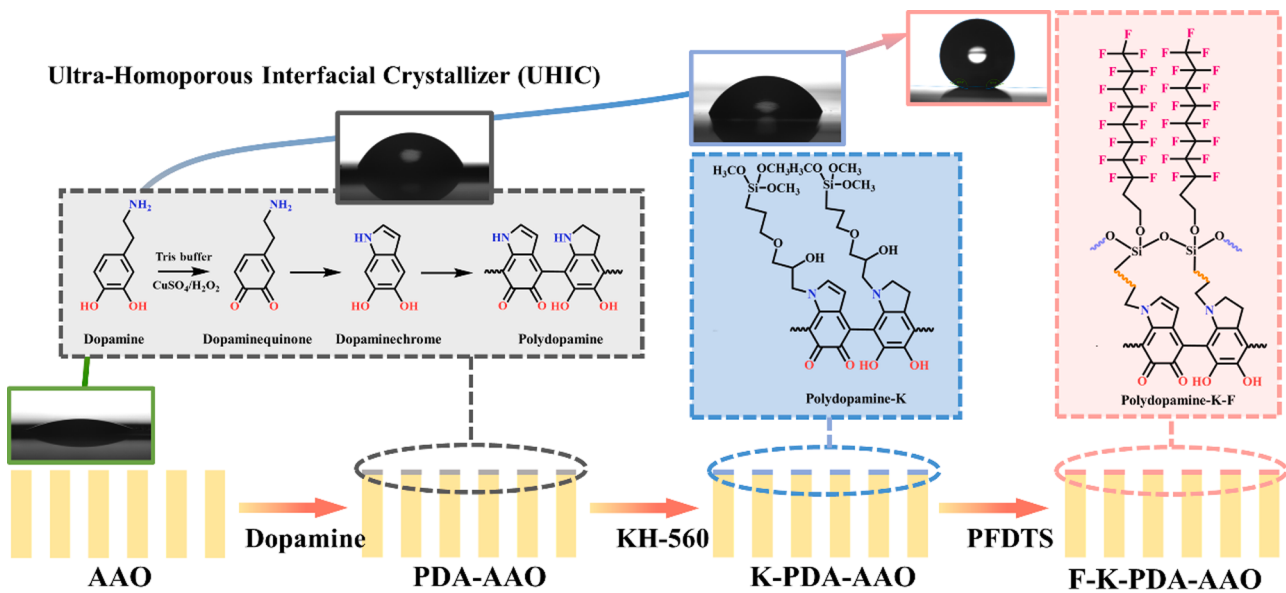


Fig. 1. Schematic diagram of the UHICs preparation.

components, and change the nuclear energy barrier of crystal [26, 30, 31]. Additionally, precise regulation of PNC pathway by constructing effective pre-cluster diffusion is also the core concern in the relevant flow chemistry and surface chemistry research [32–37]. While, the existing crystallizer commonly showed uneven surface structure and disordered tortuous channels. Heterogeneous of supersaturation degree distribution on the interface resulted in explosive nucleation and poor crystal products properties. Recently, the microporous structure and membrane with tunable pore channel and network aiming for stable gas transfer, liquid separation had been reported, which shed light on the development of the novel mass transfer microdevice [38, 39].

Herein, a high selective synthesis method of CaCO_3 superstructures was constructed based on the developed interfacial crystallizer with ultra-uniform mass transfer porous channel and interfacial superhydrophilicity. This ultra-homoporous interfacial crystallizer (UHIC) were introduced as a new biomimetic mineralization microdevice to accurately control the Gas-Liquid interfacial CaCO_3 reactive crystallization. This synthesis method allowed modulating the rate of CO_2 supply through the uniform channels to the Gas-Liquid interface on UHIC, which provided tunable interfacial nucleation surface energy and nucleation driving force. The influence of the different experimental conditions (surface energy of microscale interfacial crystallizer, CO_2 gas flow rate and CO_2 atmosphere) on the crystallization outcome were then systematically investigated. High selective construction of CaCO_3 crystal superstructure on UHIC could help to learn the nature of crystallization, and open new insights into the synthesis of biomaterials with target superstructure.

2. Materials and methods

2.1. Preparation of superhydrophobic ultra-homoporous interfacial crystallizers

Superhydrophobic UHIC were synthesized by deposition of dopamine and surface fluorination of the PFDTs on AAO membranes (Fig. 1). Dopamine hydrochloride was added into Tris-HCl solution with a concentration of 2.0 g L^{-1} . Pristine AAO membranes were immersed in the freshly prepared dopamine solution and shaken with a speed of 150 rpm at 25°C for a certain time. After that, the PDA-AAO membranes were washed using DI water and dried in the oven for 60 min at 60°C . Secondly, the PDA-AAO membranes were immersed into 2.0% wt KH560/ethanol solution at 80°C for 8 h and then washed using ethanol. The K-

PDA-AAO membranes were obtained after drying in the oven for 2 h at 60°C . Finally, the prepared K-PDA-AAO membranes were placed in the PFDTs/ethanol (0.25% wt) solution for 24 h. F-K-PDA-AAO membranes were washed using ethanol and dried in the oven for 3 h at 80°C . The resultant interfacial crystallizers were designated as $F_n\text{-AAO}$, where n represented the contact angle of interfacial crystallizers. For example, $F_{92}\text{-AAO}$ referred to the contact angle of interfacial crystallizer of 92° , i.e.

2.2. Characterization of UHICs

X-ray Photoelectron Spectroscopy (XPS, XL30, Philips Co.) were used to study the chemical structure of superhydrophobic ultra-homoporous interfacial crystallizers. The surface and cross-section morphology, roughness, superhydrophobicity and zeta potential were observed by the scanning electron microscopy (SEM, Nanosem 430), atomic force microscopy (AFM, Multimode 3, Bruker Co.), contact angle goniometer (JC2000C, China) and SurPASS Electrokinetic Analyzer (Anton Paar KG, Austria), respectively. The solid surface energy (γ_s), its dispersion component (γ_s^d) and polarity component (γ_s^p) of UHICs are calculated by using Owens Wendt Kaelble (OWK) model formula:

$$\gamma_s = \gamma_s^d + \gamma_s^p \quad (1)$$

$$\gamma_1(1 + \cos\theta) = 2\sqrt{\gamma_s^p\gamma_1^p} + 2\sqrt{\gamma_s^d\gamma_1^d} \quad (2)$$

where γ_1 , γ_1^d and γ_1^p were the surface energy, dispersion force component and polarity force component of the test solution, respectively. The solid surface energy was calculated by using deionized water as polar detection solution and Diiodomethane as nonpolar detection solution in this work. The surface energy parameters of each test solution were shown in Table S1.

2.3. Reactive crystallization on UHICs

The performance of the prepared superhydrophobic UHICs in CaCO_3 crystallization was tested by ammonium carbonate decomposition/ CO_2 diffusion technique. This method relied on the decomposition of ammonium carbonate to produce CO_2 and ammonia gas and the diffusion of CO_2 into a calcium chloride solution. The chemical reaction can be exemplified as:

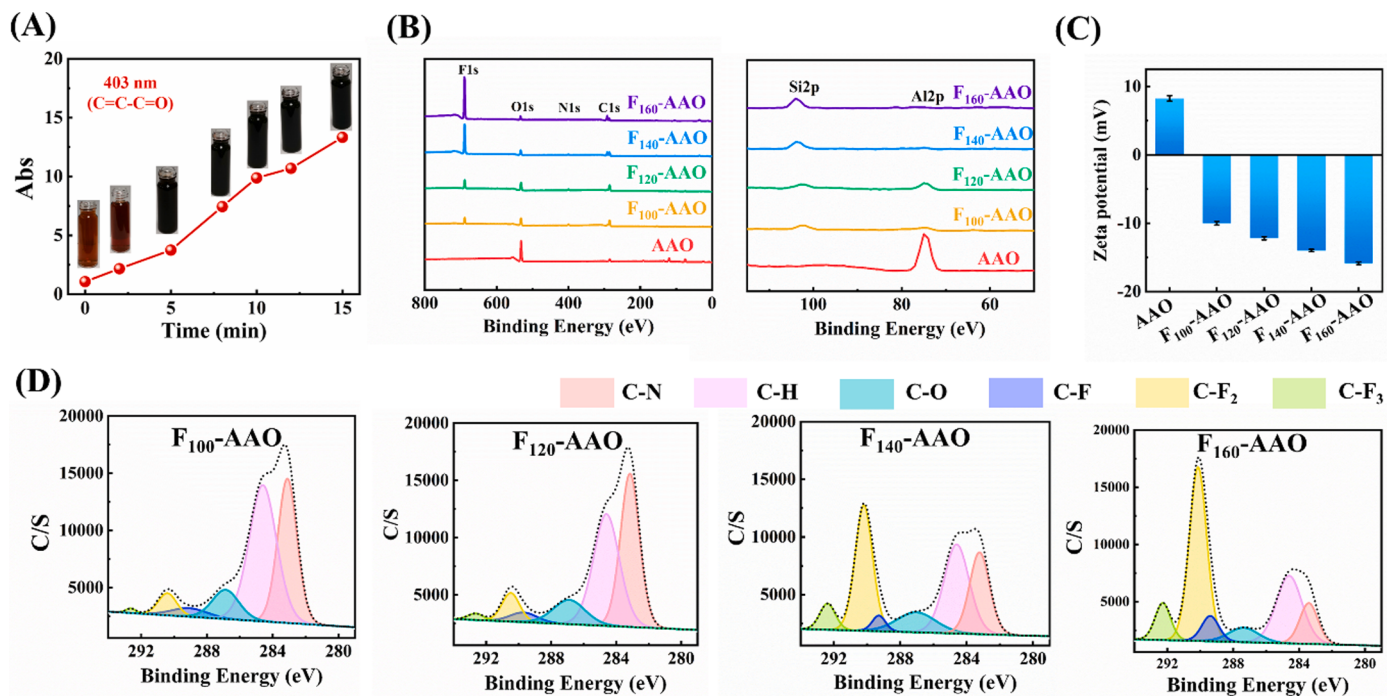
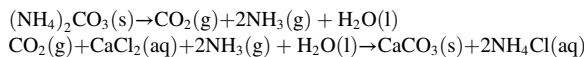


Fig. 2. (A) time-dependence of UV-vis absorbance at 403 nm for dopamine solutions; (B) XPS; (C) Zeta potential; (D) C1s core-level spectrum resolving results of UHICs.



The decomposition rate x (%/min) of ammonium carbonate at different temperatures was measured by Thermogravimetric (TG) analyzer,

$$x = \frac{\omega_0 - \omega_1}{\Delta t} \quad (3)$$

where ω_0 and ω_1 are the initial percentage and residual percentage of $(NH_4)_2CO_3$, respectively. Δt (min) is the decomposition time of $(NH_4)_2CO_3$.

The molar decomposition rate of ammonium carbonate $n_{(NH_4)_2CO_3}$ (mol/min) is calculated as follows:

$$n_{(NH_4)_2CO_3} = \frac{mx}{M_{(NH_4)_2CO_3}} \quad (4)$$

where m and $M_{(NH_4)_2CO_3}$ are the weight m (g) and molar mass (g mol⁻¹) of ammonium carbonate, respectively.

According to the decomposition equation of ammonium carbonate, the molar decomposition rate of ammonium carbonate is equal to the molar formation rate of carbon dioxide n_{CO_2} (mol/min),

$$n_{(NH_4)_2CO_3} = n_{CO_2} \quad (5)$$

and then the carbon dioxide gas flow rate Q_{CO_2} (L/min) was calculated:

$$Q_{CO_2} = n_{CO_2} V_m = \frac{mx}{M_{(NH_4)_2CO_3}} V_m \quad (6)$$

where V_m is the molar volume of gaseous CO_2 (L mol⁻¹). The gas flow rate Q_{CO_2} (L/min) of CO_2 were shown in Table S2.

The mineralization test was the crystallization at superhydrophobic ultra-homoporous interfacial crystallizer/solution/air interface. Specifically, a drop of $CaCl_2$ solution (5 mM) was placed on the superhydrophobic side of the ultra-homoporous interfacial crystallizer. The droplets were stable on the surface of the superhydrophobic ultra-homoporous interfacial crystallizer, and $CaCO_3$ particles form at the interface of the interfacial crystallizer /solution. The back surface of the

interfacial crystallizer was exposed to the CO_2 gas stream generated by the decomposition of solid ammonium carbonate for a certain time. In all mineralization experiments, CO_2 diffused to the interfacial crystallizer interface through the pore channels, and then reacted with calcium ions to form $CaCO_3$ particles.

2.4. Characterization of $CaCO_3$ crystals

The physical and chemical characterization of $CaCO_3$ crystals, including morphology, chemical structure and crystallinity, were conducted using SEM, EDS, Fourier transform infrared (FTIR, Nicolet 560) spectrometer, and XPS, respectively. The crystalline structure of $CaCO_3$ crystals obtained at different gas flow rate was characterized by X-ray diffractometer (XRD, Rigaku D/Max-2500/PC) analysis to confirm the crystal forms of different morphologies. The molar content (%) of $CaCO_3$ polymorphs can be calculated according to the intensity of the (104) plane of calcite and the (110) plane of vaterite:

$$X_V = \frac{7.691I_V^{110}}{I_C^{104} + 7.691I_V^{110}} \quad (7)$$

where X_V and X_C are the molar content (%) of vaterite and calcite, respectively. I_C^{104} and I_V^{110} are the XRD intensity of the (104) and (110) plane of calcite and vaterite.

3. Results and discussion

3.1. Characterization of UHICs

In this work, the grafting rate of fluorine-containing segments provided a higher regulation for the superhydrophobic modification of UHICs. Dopamine was generally oxidized under alkaline conditions and spontaneously self-polymerizes to construct an ultrathin and surface-adhering polydopamine coating. The color of dopamine solution turned black gradually with the prolongation of deposition time attributed to the production of reactive oxygen species (ROS) in dopamine solution by Cu^{2+} and H_2O_2 , which helped to promote the oxidation of dopamine. The extent chemical reactions were suggested by UV-vis

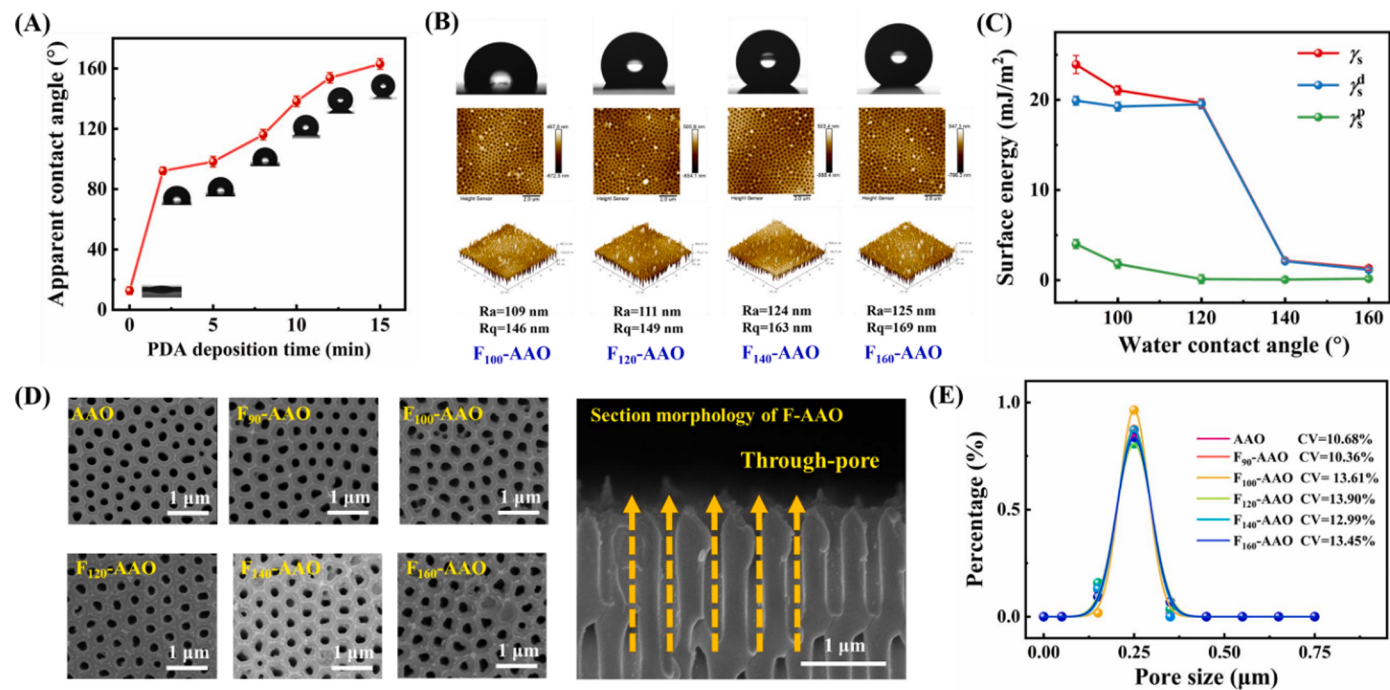


Fig. 3. Physical structure characterization of hydrophobic UHIC: (A) Water contact angle; (B) Roughness; (C) Surface energy parameters of interfacial crystallizer surfaces; (D) The SEM surface and cross-section morphologies; (E) Pore size distribution.

spectra of the dopamine solutions (Fig. 2A). The absorption at around 403 nm was attributed to the polymerization of dopamine (C-C-C=O) and the absorption at 403 nm gradually increased to 13.33, indicating the deposition process triggered by $\text{CuSO}_4/\text{H}_2\text{O}_2$. XPS spectra was performed to analyze the chemical bonding and the surface elements of UHICs (Fig. 2B). Compared with the pristine AAO membrane, all the superhydrophobic UHICs presented three peaks at 689 eV (F 1s), 400 eV (N 1s) and 102 eV (Si 2p), indicating the successful introduction of fluorine-containing chains on the surface of pristine AAO membranes. The elemental atomic percentages of aluminum (Al), oxygen (O), carbon (C), nitrogen (N), silicon (Si) and fluorine (F) on the interfacial crystallizer surface were listed in Table S3. With the prolongation of dopamine deposition time, the content of fluorine element in the separation layer gradually increased. With the extension of dopamine deposition time, the original AAO interface is covered by fluorine-containing coating, and the interface elements gradually change from O and Al on the AAO interface to F, C, O, N and Si on the fluorine-containing chain segment. The aluminum and oxygen content on the fluorine-containing chain segment is much lower than that on the AAO membrane. Therefore, the introduction of a large amount of fluorine reduces the content of chlorine and oxygen at the interface. The surface charge character of the as-prepared superhydrophobic UHIC with different grafting ratio of fluorine chains was evaluated by the zeta potential and presented in Fig. 2C. Zeta potential of the pristine AAO membrane was 8.26 mV, which was higher than that of all the F-AAO interfacial crystallizer. As the deposition time of dopamine increased from 2 to 15 min, the electronegative zeta potential reduced from -9.99 mV ($F_{100}\text{-AAO}$) to -15.85 mV ($F_{160}\text{-AAO}$), which was attributed to the electronegative charge of C-F moieties on the surface and physical adsorption of hydroxide ions. In principle, negatively charged groups could increase the migration rate of Ca^{2+} ions from the solution to the interface, contributing to promote the nucleation of crystals. According to the high-resolution C1s XPS spectra of the interfacial crystallizers (Fig. 2D and Table S4), the proportion of C-F₃ bond increased from 0.55% to 8.24%, further verifying the increase in the grafting ratio of fluorine chains.

The water contact angle is important to reflect the micro contact state between the droplet and porous interface, which was of great

Table 1

The apparent water contact angle (θ), roughness area ratio (r) and corrected water contact angle (θ' , $\cos\theta' = \cos\theta/r$) of UHICs.

UHICs	θ (°)	surface area (μm^2)	Projected area (μm^2)	r	θ' (°)
AAO	15.7 ± 0.6	252	100	2.52	67.2 ± 0.9
$F_{100}\text{-AAO}$	100.0 ± 2.0	221	100	2.21	94.5 ± 0.9
$F_{120}\text{-AAO}$	120.0 ± 2.0	234	100	2.34	102.3 ± 0.8
$F_{140}\text{-AAO}$	140.0 ± 3.0	238	100	2.38	108.8 ± 0.8
$F_{160}\text{-AAO}$	160.0 ± 3.0	255	100	2.55	111.6 ± 0.4

significance for the coordinated control of nuclear barrier and micro-scale diffusion region. The apparent water contact angle on UHIC gradually increased with the prolongation of dopamine deposition time, resulting in the superhydrophobic interface (Fig. 3A). The apparent water contact angles (θ) were influenced by the intrinsic hydrophobicity and roughness of UHICs. As shown in Fig. 3B, the roughness of hydrophobic UHIC surface (R_{ms}) slightly increased with the enhancement of water contact angles from 109 nm to 125 nm. And the influence of roughness could be described by the Wenzel model, which is represented as $\cos\theta' = \cos\theta/r$, where θ' was the corrected water contact angles, and r was roughness area ratio. The parameters (θ , surface area, projected area, r and θ') of interfacial crystallizers were presented in Table 1. The apparent water contact angles of pristine AAO ultra-homoporous membrane was 15.7° . After hydrophobic modification, the apparent water contact angle increased significantly to 160° due to the introduction of fluorine-containing chains and the increase of surface area. Eliminated the influence of roughness on water contact angle, the corrected water contact angles increased from $94.5 \pm 0.9^\circ$ to $111.6 \pm 0.4^\circ$ (Table 1). The results indicated that the rough structure and fluorine-containing groups synergistically enhanced the superhydrophobic properties of UHICs. Solid surface energy is an important parameter of

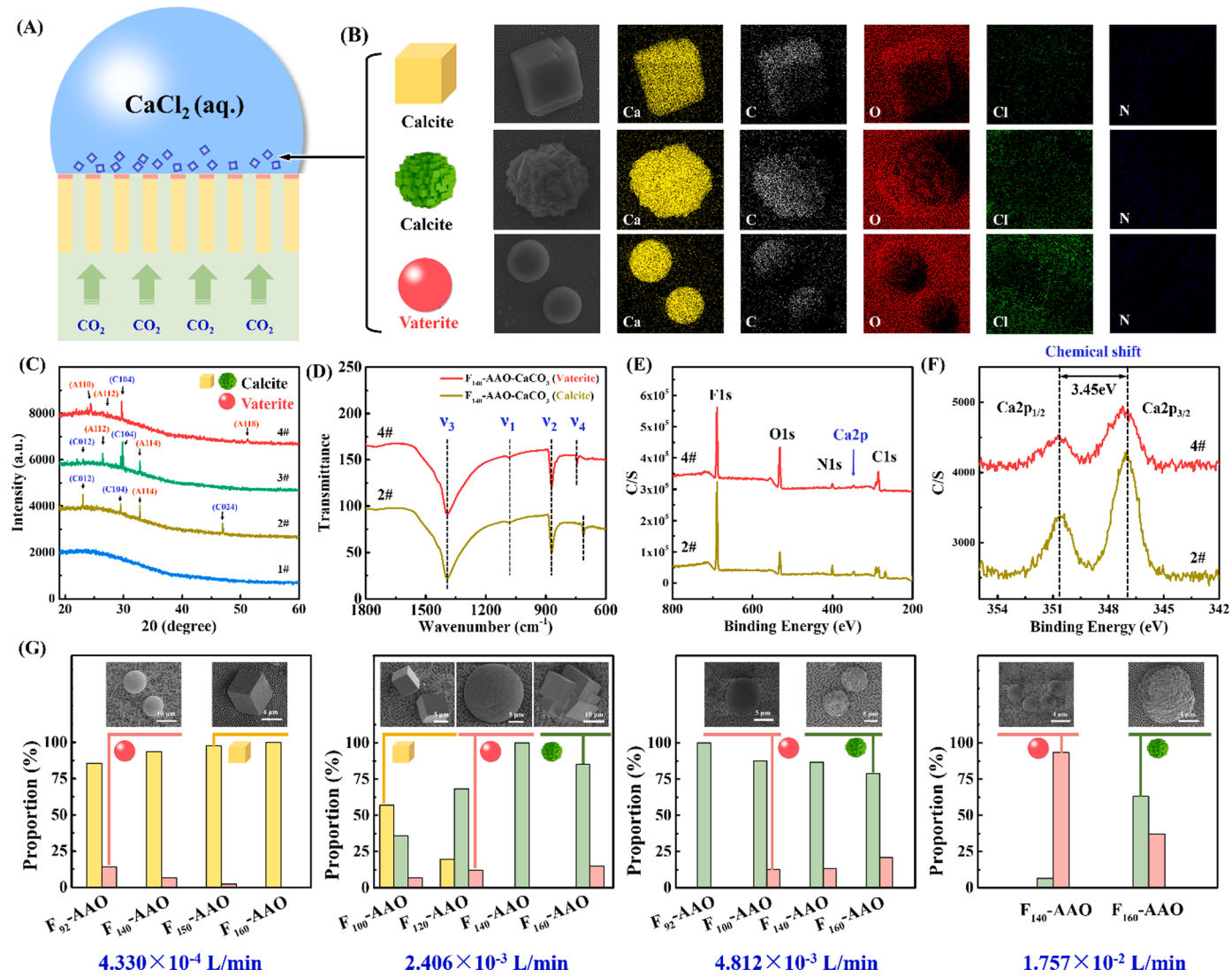


Fig. 4. (A) Effect of gas flow rate on UHIC crystallization: schematic diagram of the experiments; (B) Mapping of classic CaCO_3 crystal morphologies obtained; (C) XRD of $\text{F}_{140}\text{-AAO}$ UHIC (1#) and CaCO_3 crystals obtained at different gas flow rate: $3.69 \times 10^{-5} \text{ m/h}$ (2#); $4.06 \times 10^{-4} \text{ m/h}$ (3#); $4.06 \times 10^{-3} \text{ m/h}$ (4#); (D) FTIR spectra; (E) XPS spectra of CaCO_3 crystals; (F) Ca core-level XPS spectra of CaCO_3 crystals; (G) Proportion of CaCO_3 crystals under different gas flow rate.

the intrinsic hydrophobicity [40]. The solid surface energy(γ_s), its dispersion component(γ_s^d) and polarity component(γ_s^p) of UHICs are calculated by using Owens Wendt Kaelble (OWK) model, as shown in Fig. 3C. The surface energy of hydrophilic UHICs was the highest (71.28 mJ/m^2), and the fluorine-containing segments are highly hydrophobic and nonpolar. When the hydrophilic AAO membrane was grafted onto the surface of the homoporous membrane, the polar component of the surface energy of the UHICs was significantly reduced to 1.32 mJ/m^2 with the increase of water contact angle. Hydrophobic is an important factor to ensure the stable existence of droplets at the interface, which could ensure that the gas-liquid reaction crystallization process was carried out at the interface of UHICs. Furthermore, for future potential applications, including continuous processes of reactive crystallization, antisolvent crystallization and distillation crystallization, hydrophobic interface would be not only used as heterogeneous nucleation interface, but also as the mass transfer device for solvent concentration and the interfacial hydrophobicity was a necessary condition to ensure mass transfer efficiency.

In addition, SEM was utilized to analyze the surface and cross-section morphology of the investigated UHICs, as shown in Fig. 3D. All the interfacial crystallizer surfaces showed the ultra-homoporous structures

exhibiting a sharp pore size distribution (C.V. $\leq 13.90\%$) with the pore radius of $220 \pm 10 \text{ nm}$ and regular pore spacing of $490 \pm 10 \text{ nm}$ (Fig. 3E), which was conducive to the uniform distribution of supersaturation at the interface. Besides, no obvious blockage was found on the interfacial crystallizer surface and the channel of interfacial crystallizer was still the high precise and parallel microchannel, which could provide a good foundation for each channel to maintain stable gas transfer and even average gas flow rate on the whole interface, ensuring the feasible and high accuracy gas diffusion.

3.2. Interfacial crystallization on UHICs under different operation modes

The UHIC with ultra-uniform channel size distribution and tunable interfacial nucleation energy was used as the crystallization loading platform. Diverse operation modes can be achieved. One type of interfacial crystallization is the sessile CaCl_2 droplet located on the interface of UHICs, which covering all the interface channels. The CO_2 gas flow contacted the liquid phase only through the channel and realized the Gas-Liquid interfacial reactive crystallization in confinement (Fig. 4A). This operation mode can directly reveal the mechanism that how gas flow rate impacts on the interfacial crystallization occurred on UHIC.

Different morphologies of CaCO_3 , including cubic, polyhedron and

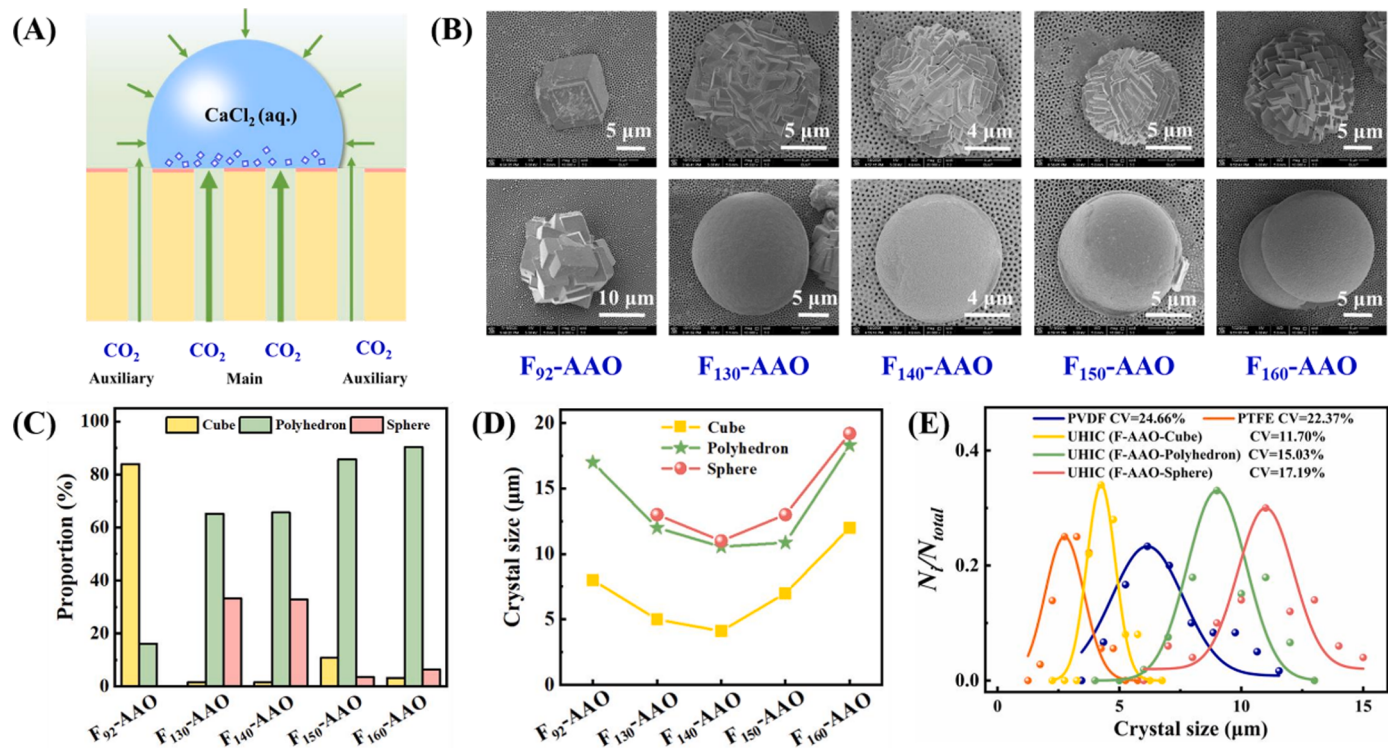


Fig. 5. (A) UHIC with diverse superhydrophobicity for CaCO₃ crystallization under hybrid CO₂ gas atmosphere: Schematic diagram of the experiments; (B) Typical CaCO₃ crystal morphologies obtained; (C) Proportion of CaCO₃ crystals with different morphologies; (D) Average particle size and (E) particle size distribution of CaCO₃ crystals obtained.

sphere, were successfully synthesized under different CO₂ gas flow rate (range from 4.330×10^{-4} L/min to 1.757×10^{-2} L/min) on the developed UHICs, as shown in Fig. S1 to S4. The EDX-mapping of representative crystal morphologies showed the enrichment of calcium (Ca), carbon (C) and oxygen (O) elements except for chlorine (Cl), which confirmed that the crystals were CaCO₃ (Fig. 4B). Crystalline structure of CaCO₃ was characterized by XRD analysis. As presented in Fig. 4C, the characteristic peaks of cubic crystals at 2θ of 23.49, 29.41 and 46.94 correspond to the (012), (104) and (024) crystallographic planes of calcite. The spherical crystals obtained at ultra-high gas flow rate (1.757×10^{-2} L/min) correspond to the (110), (112) and (118) crystallographic planes of vaterite at 2θ of 24.40, 27.27 and 50.04, respectively. Combined with the crystal morphology (Fig. S1 to S4), it could be determined that spherical CaCO₃ was vaterite, while cubic and polyhedral CaCO₃ were calcite. With the increase of CO₂ gas flow rate from 4.330×10^{-4} L/min to 1.757×10^{-2} L/min, the molar content of vaterite increased to more than 80% (Table S5). The chemical structures of CaCO₃ crystals were measured by the FTIR and XPS spectrometer. The vibrational bands at 1390, 1080, and 876 cm⁻¹ can be clearly assigned to the asymmetric stretch of the carbonate ion (ν_3), carbonate symmetric stretching (ν_1), carbonate out-of-plane bending (ν_2), respectively. The cubic crystal obtained at low Q_{CO₂} showed calcite characteristic peak at 713 cm⁻¹ corresponding to inplane bending (ν_4) vibrations (Fig. 4D). However, the characteristic peak shifted to 745 cm⁻¹ attributing to the enhancement of spherical crystal proportion at super high Q_{CO₂}. The XPS spectra of CaCO₃ crystals showed five characteristic peaks of 689.54 eV (F1s), 532.55 eV (O1s), 401.49 eV (N1s), 347.04 eV (Ca2p) and 292.23 eV (C1s). As the characteristic element of CaCO₃ crystals, Ca core-level XPS spectra showed a double spin peak, in which Ca2p_{3/2} at 347.25 eV and Ca2p_{1/2} at 350.70 eV (Fig. 4F). The intensity ratio of the double peak was 2:1, and the chemical shift between the core level of Ca2p_{3/2} and Ca2p_{1/2} was 3.45 eV, which was consistent with that of CaCO₃ reported in the literature [41, 42].

As shown in Fig. 4G, it was found that cubic crystals with diameters

of 8 μm were mainly formed at low CO₂ gas flow rate, the proportion of which remained above 80%. Increasing the CO₂ gas flow rate to 2.406×10^{-3} L/min, the proportion of spherical crystals increased to more than 90% and the cubic crystal gradually decreased, which presented a high selectivity on the spherical crystal. Meanwhile, the polyhedral CaCO₃ crystals (25 μm) were obtained, which possessed layered structures composed of 2.5 μm single particles or larger aggregates. With the further increase of CO₂ gas flow rate to 4.182×10^{-3} L/min, the morphologies of CaCO₃ crystals were polyhedron and sphere, and the cubic crystals disappeared completely. The size of the cuboid unit of polycrystalline aggregate became smaller and uniform. At super high CO₂ gas flow rate (1.757×10^{-2} L/min), the proportion of polyhedron and sphere CaCO₃ increased significantly to 90%, 10 times higher than that of low CO₂ gas flow rate. These results indicated that different morphologies of CaCO₃ could be constructed by simply adjusting the CO₂ gas flow rate on the developed UHICs, which provide a promising approach to improving the poor morphology selectivity prepared by multiphase reaction crystallizer or other G-L biphasic methods [43-47].

In principle, the formation process of CaCO₃ was usually involved into three stages. First, CO₂ dissolved into CaCl₂ solution to form HCO₃²⁻ and CO₃²⁻, then diffused into the solution and combined with Ca²⁺ to produce supersaturated state. And the amorphous calcium carbonate (ACC) formed as the supersaturation reached the critical value [5, 48]. Subsequently, CO₃²⁻ was continuously generated to make the supersaturation of the solution reach the required level for nucleation, and ACC was dissolved to form metastable crystals. Finally, that metastable crystals was dominated by the Ostwald ripening to form more stable calcite. UHICs was introduced to rationally control both local supersaturations in the vicinities of different CO₂ gas flow rate and subtle variations in the lattice mismatch between the mineralization interfacial crystallizer and the nucleus. At low CO₂ gas flow rate, CO₃²⁻ could not be replenished in time after reacting with Ca²⁺, and the conductivity of the solution decreased rapidly, resulting in rapid nucleation of CaCO₃ and obtaining cubic crystals. With the increase of

CO_2 gas flow rate, the decrease of $\text{Ca}^{2+}/\text{CO}_3^{2-}$ ratio could promote the formation of vaterite and inhibit the transformation to calcite. Besides, ammonium carbonate, as a CO_2 source, could also decompose into NH_3 at the same time, and its molar mass was twice than that of CO_2 . The decomposed NH_3 dissolved in solution and hydrolyzed to NH_4^+ . Excess NH_4^+ ions were adsorbed on the surface of vaterite, which stabilized the existence of vaterite. In addition, the existence of NH_4^+ ions made the system had buffering capacity and kept the conductivity stable during the formation of CaCO_3 crystals, resulting in prolonging the induction time from supersaturation to nucleation and slowing the nucleation of CaCO_3 crystal. Thus, the coordination among ion diffusion, ACC formation and particle growth rate was realized by the accurate fabricated UHIC. Under the same gas flow rate, the nanoscale channel possessed more intense micro-disturbance intensity, more uniform local diffusion and smaller concentration gradient compared to the submillimeter scale channel in conventional microfluidic or tubular crystallizer. Therefore, based on the ultra-homo parallel microchannels and ultra-uniform channel spacing distribution, UHICs showed the characteristics of the ultra-uniform 200 nm level channel array for gas transmission and supersaturation control. The high selective switching and controlled synthesis between cubic-polyhedral-spherical superstructure could be realized on the UHICs only by adjusting the CO_2 gas flow rate.

To additionally reveal the engineering performance of UHIC under different G-L reactive crystallization condition, UHIC with diverse superhydrophobicity were implemented in the mineralization process under the hybrid CO_2 gas atmosphere. CaCl_2 aqueous droplets were stable on the interface of UHICs and the droplets partially covered the interface nanoscale channels. Thus, the gas could enter the liquid phase through two pathways which was different from the previous experiments. One is that the gas directly entered the liquid phase through the UHICs channel, and the other is that the gas entered the gas-phase environment around the droplets through the UHICs channel to create CO_2 atmosphere, and then entered the liquid phase, realizing the reactive crystallization at the Gas-Liquid interface (Fig. 5A).

The interfacial superhydrophobicity of UHIC illustrated a great influence on the morphology selectivity of CaCO_3 with high CO_2 gas flow rate (4.812×10^{-3} L/min). When the interfacial solution contract angle ranged from 92° to 160° , three typical morphologies of CaCO_3 crystals were also obtained with desire selectivity (Fig. 5B and Fig. S5). Cubic crystals with diameters of 8 μm were mainly formed at low contact angle, the proportion of which remained above 80% (Fig. 5C). With the increase of surface hydrophobicity to 160° , the proportion of cubic CaCO_3 crystal decreased to less than 5%, while the proportion of polyhedral CaCO_3 crystals (18 μm) were increased to more than 90%. The proportion of spherical and polyhedral crystals increased by 6 times (from 16.1 % to 96.77 %) with the reduction of surface energy. As shown in Fig. 5D, the particle size of spherical and polyhedral crystals was larger than that of cubic crystal due to the different relative values of nucleation rate and growth rate. Compared with cubic crystals, spherical and polyhedral crystals were usually obtained at a higher nuclear barrier, showing low nucleation rate. The increased nucleation barrier could limit the number of nuclei and guide the growth of nuclei, resulting in larger crystal size of spherical and polyhedral crystals. The size of the cuboid unit of polyhedral crystals became smaller and uniform than that of crystals obtained at air atmosphere (Fig. 5D and 5E), which indicated a higher nucleation rate and uniform growth rate. These results indicated that different morphologies of CaCO_3 could be obtained by adjusting the interfacial superhydrophobicity of UHIC, which revealed the key parameter of this proposed new-type crystallizer.

Under the same conditions, the mineralization experiments were carried out on the commercial polymer microporous membranes as the microscale gas distributor (with similar average pore size) and interfacial crystallizer, including Poly tetra fluoroethylene (PTFE), Polyvinylidene fluoride (PVDF) and polypropylene (PP) for they are typical materials widely used in surface crystallization as the microscale gas distributor owing to the excellent structural stability and high permeate

flux. The surface of commercial polymer microporous membranes showed irregular pore structure, which was not conducive to the uniform distribution of interfacial supersaturation. As shown in Fig. S6, the crystal morphology was mainly cubic and only a few spherical crystals (<15%) appeared on the PVDF membrane. Meanwhile, the uniformity of crystal size distribution of commercial microporous membrane was worse than that of UHICs and it was difficult to control the proportion of crystals with different morphologies (Fig. S6). The crystallization experiments further confirmed that UHICs has the prominent advantages over commercial microporous membranes in high selective synthesis of CaCO_3 superstructures and uniformity of crystal size distribution (Fig. 5E and Table S6).

3.3. Principles and fundamental theory of CaCO_3 crystallization on UHIC

The principles of UHIC for accurate engineering the CaCO_3 superstructure synthesis should be illustrated from the kinetics and thermodynamics aspects, which is important for the rational design of UHIC and further investigation. The transfer characteristics of interfacial crystallizer are closely related to its inherent micropore structure, including pore size, pore size distribution and channel curvature. The separation effect of gas in microporous interfacial crystallizer is determined by the Knudsen number, which was calculated as follows,

$$K_n = \frac{\lambda}{d_p} \quad (8)$$

where λ is the mean free path of gas molecules, and d_p is the average pore size of interfacial crystallizers.

Herein, the mean free path of CO_2 is 62.9 nm in the standard state and the average pore size of the UHIC is 220 nm. The calculated K_n is 0.28, which is slightly less than 1, that is, the molecular flow in the pore is mainly dominated by the collision between molecules, and the transfer characteristics are between Knudsen flow ($K_n << 1$) and viscous flow ($K_n >> 1$). According to Hagen-Poiseuille formula, the standard volume flow (Q_V) through the interfacial crystallizer pore can be obtained [49]. The formula is as follows:

$$\frac{dp}{dx} = -\frac{8RT\mu N}{P\pi r^4} \quad (9)$$

where p , x and r are gas pressure, gas flow direction and pore radius, respectively. Assuming that the direction of the pore is perpendicular to the interfacial crystallizer surface and the pressure p_h and p_L on both sides of the pore are fixed, the total molar flow of gas through the pore N is calculated as follows:

$$N = \frac{\int_{p_h}^{p_L} \frac{1}{2}\pi r^4 d(p^2)}{\int_0^L -8RT\mu L \, dL} = \frac{\pi r^4 (p_h^2 - p_L^2)}{16RT\mu L} \quad (10)$$

where L is the thickness of interfacial crystallizer, and N is converted into the standard volume flow (Q_V) through the interfacial crystallizer,

$$Q_V = \frac{NRT}{P} = \frac{\pi r^4 p^* \Delta p}{8T^* \mu L} \quad (11)$$

For real interfacial crystallizer materials, the channel has a more complex network structure. The gas transmission length is much longer than the interfacial crystallizer thickness, and the tortuosity factor τ_T is introduced. The modified L^* value is as follows:

$$L^* = L\tau_T \quad (12)$$

Then the formula can be written as:

$$Q_V = \frac{NRT}{P} = \frac{\pi r^4 p^* \Delta p}{8T^* \mu L^*} \quad (13)$$

Owing to the ideal straight through channel, the tortuosity factor (τ_T) of UHICs was approximately equal to 1. While, the tortuosity factor (τ_T)

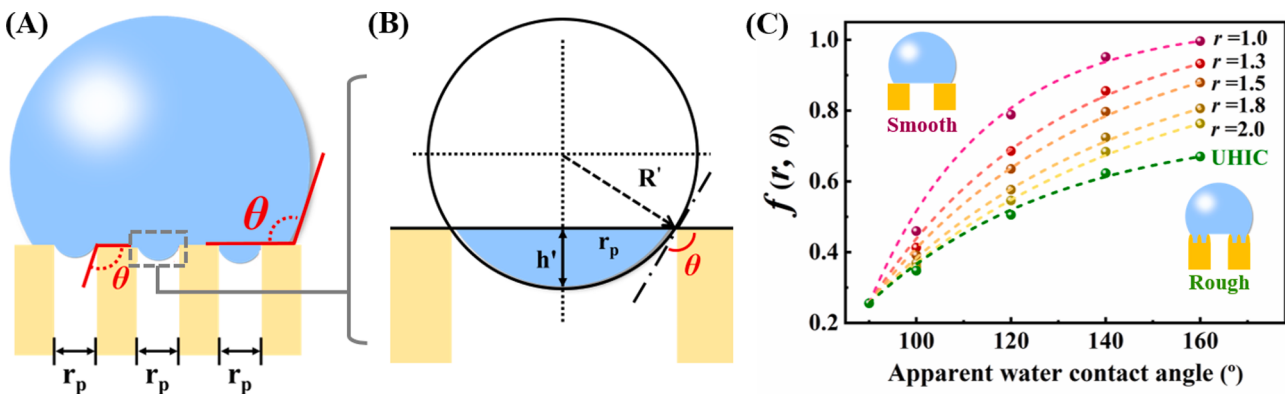


Fig. 6. (A) The contact angle θ between the heterogeneous surface and the crystallizing solution.; (B) Geometry of the sphere cap of a drop inside a pore of the interfacial crystallizer; (C) Impact of different hydrophobicity and roughness area ratio on interfacial nucleation correlation coefficient ($f(r, \theta) = \Delta G_{\text{Heter}}^*/\Delta G_{\text{Homo}}^*$);

of commercial microporous membrane was much larger than 1. The increase of tortuosity factor resulted in much longer gas transmembrane path and then increased the mass transfer resistance, which was not conducive to the effective transmission of gas and reduced the standard volume flow (Q_V). In addition, compared with the crystallization at the interface of UHIC, the difference of commercial polymer microfiltration membrane pore size (r) led to the inconsistency of local CO_2 gas flow rate in different pores, causing the uneven local supersaturation of CaCO_3 on the interfacial crystallizer. Thus, we can predict the inconsistent nucleation and poor uniformity of crystal size distribution on the microporous membrane.

The nucleation barrier is determined by the complex interaction between physical and chemical parameters. Free energy for critical nucleus formation, given by the difference between the energy gained upon the formation of a bulk phase and the energy required to form new surface area, is a crucial parameter in nucleation theory. The wetting behavior of rough surfaces is usually described by the Wenzel equation:

$$(\gamma_{sf} - \gamma_{sc}) / \gamma_{cf} = \frac{1}{r} \cos \theta \quad (14)$$

where r is the roughness area ratio, as presented Table 1. For rough porous surfaces, the effect of foreign bodies on lowering the nucleation barrier can be quantified by an interfacial correlation factor $f(r, \theta)$, which is defined as:

$$f(r, \theta) = \frac{\Delta G_{\text{Heter}}^*}{\Delta G_{\text{Homo}}^*} = \frac{\left(2 + \frac{1}{r} \cos \theta\right) \left(1 - \frac{1}{r} \cos \theta\right)^2}{4} \left[1 - e^{-\frac{\left(1 + \frac{1}{r} \cos \theta\right)^2}{\left(1 - \frac{1}{r} \cos \theta\right)^2}}\right]^3 \quad (15)$$

(refer to Fig. 6A and Fig. 6B for the meaning of the additional geometric parameters), where ΔG_{Homo}^* is the homogeneous nucleation barrier, and $\Delta G_{\text{Heter}}^*$ is the heterogeneous nucleation barrier; $f(r, \theta)$ is the interface correlation coefficient, which indicated the reduction of the nucleation barrier due to the presence of rough porous surfaces; θ is the apparent water contact angle.

According to the formula of heterogeneous nucleation barrier at porous surfaces, the nucleation barrier at different hydrophobic and roughness area ratio interfaces was calculated as shown in the Fig. 6C. With the increase of apparent water contact angle (θ) range from 100° to 160°, the correlation coefficient of nuclear barrier interface increased gradually. The high nucleation barrier made it difficult for ACC to construct stable cubic crystals in one step. Thus, forming metastable polyhedrons and spheres. The enhancement of nucleation barrier could delay the formation of stable crystal phase of CaCO_3 , so as to effectively controlled the proportion of metastable CaCO_3 and realize the high selective synthesis of CaCO_3 superstructures. Compared with the

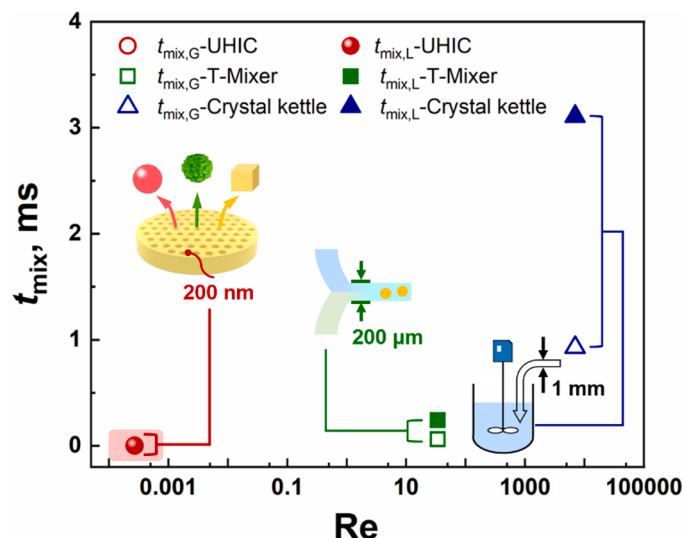


Fig. 7. Theoretical interfacial mixing time ($t_{\text{mix}, G}$ for gas phase and $t_{\text{mix}, L}$ for liquid phase) of CO_2 versus Reynolds number in different microscale devices (UHIC, classic T-Mixer, crystal kettle).

hydrophilic interface, the superhydrophobic interface reduced the dynamic persistence of ACC due to the weak interaction between the water molecules in ACC and the superhydrophobic interface. With the increase of the roughness area ratio, the increase rate of the interfacial correlation coefficient gradually slowed down, which was due to that the cavity on the rough interface blocked the lateral migration of the adsorbed solute molecules, and the accumulation of solute molecules in the cavity reached supersaturation to form crystals. In addition, the reduction of heterogeneous nucleation barriers was also attributed to the rough structure providing nucleation sites.

Compared to the traditional microfluidic module or microporous membrane, the UHIC possessed ultra-uniform channel size distribution and tunable interfacial nucleation energy (ranged from 71.28 to 1.32 mJ/m²). The distinctive nanoscale ultra-homo channels render the droplet ultra-homo nucleation site with controllable nucleation barrier. In addition, this microscale channel structure is critical for the Gas-Liquid interface reaction via high-effective diffusion and micromixing.

Herein, a simplified logarithm function to describe the theoretical mixing time in different microscale devices is given by [50]:

$$t_{\text{mix}} = t_{\text{diff+shear}} = \frac{d^2 / D_i}{8Pe} \ln(1.52Pe) \quad (16)$$

where D_i is the diffusion coefficient of molecular in the corresponding

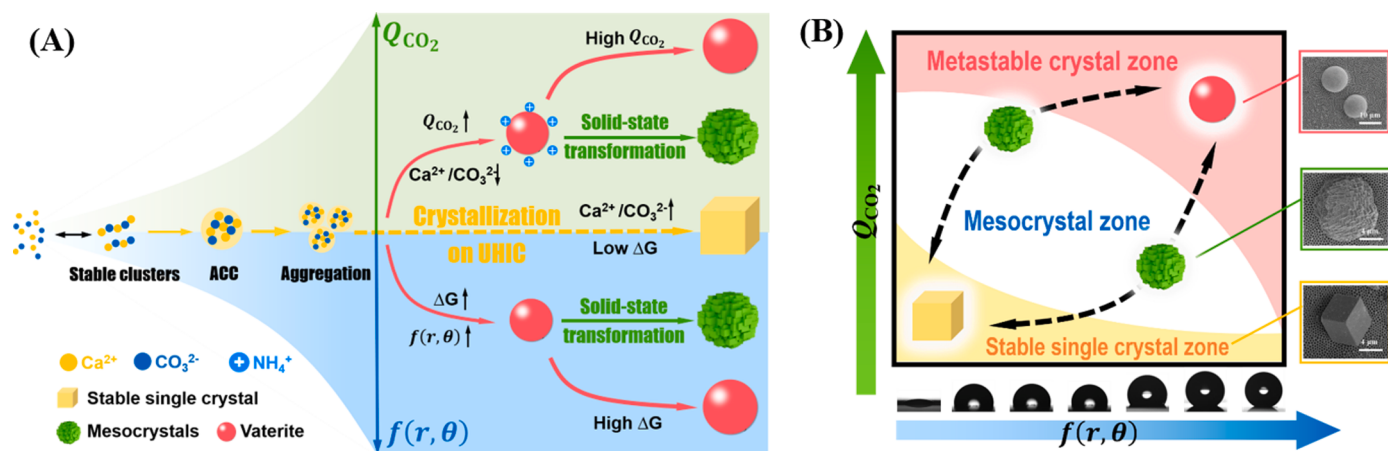


Fig. 8. (A) Schematic diagram of CaCO_3 crystal superstructures regulation via controlling gas flow rate (Q_{CO_2}) and ($f(r, \theta)$) on UHIC.

phase ($i=G$, gas phase of L, liquid phase); d is the channel diameter; Pe is the Peclet number (the constant and parameters used in the calculation are listed in supplementary materials Table S7). As shown in Fig. 7, the theoretical interfacial mixing time on the Gas-Liquid reaction interface of UHIC (the 200 nm scale channel) are both very short ($t_{\text{mix},G-\text{UHIC}}: 3.05 \times 10^{-10}$ s; $t_{\text{mix},L-\text{UHIC}}: 1.36 \times 10^{-6}$ s). The difference between $t_{\text{mix},G-\text{UHIC}}$ and $t_{\text{mix},L-\text{UHIC}}$ is so small, the two labels are almost coincident. While, as for the classic T-Mixer that the channel diameter equal to 200 μm , under the same CO_2 gas flow rate Q_{CO_2} , the gap between the theoretical interfacial mixing time increased to 10^{-4} s level ($t_{\text{mix},G-\text{T-mixer}}: 6.2 \times 10^{-5}$ s; $t_{\text{mix},L-\text{T-mixer}}: 2.4 \times 10^{-4}$ s). Considering the pre-cluster formation and nucleation process usually occurs in 10^{-9} to 10^{-6} s level, this different mixing procedure on the G-L interface may result in non-matched reaction and crystallization. This nonmatched mixing and diffusion process became more significant in the classic crystal kettle (the Rotating speed of stirring is setted to 300 rpm to ensure the turbulence flow in the crystallizer, Re is equal to 6900). The difference of interfacial mixing time on the theoretical millimeter-level CO_2 bubble in the crystal kettle increased to 2×10^{-3} s. Thus, in principle, the developed UHIC in this work possessed two key features as a desire reactive crystallizer: (1) tunable interfacial nucleation correlation coefficient ($f(r, \theta)$); (2) significantly improved micromixing and mass transfer performance.

In addition, the perfluorinated segments at the interface played a crucial role in adsorption and complexation of Ca^{2+} . When the CaCl_2 droplet contacted with the interface, the Ca^{2+} in the solution would preferentially gather near the fluorine-containing chain segments, resulting in the supersaturation of Ca^{2+} on the interface, which could react with CO_3^{2-} to form ACC. The surface solute interaction enriches the solute concentration near the surface, and the molecular recognition between the surface and solute induces the partial orientation order in the enriched solute layer; these two effects can both promote the formation of crystal nucleus. Spherical CaCO_3 microcrystals were induced to form when ACC reached local supersaturation and continued to grow under the action of microcrystal electrostatic force, finally forming uniform spherical CaCO_3 crystals, as shown in Fig. 8A. Besides, Rodriguez Navarro et al. proved that organic molecules with fluorine-containing segments could inhibit the transition from metastable spherical to stable cubic crystals [51, 52]. Therefore, the ratio of spherical and polyhedral CaCO_3 crystals increased significantly. As illustrated in Fig. 8B, the targeted preparation of CaCO_3 crystals with different morphologies was realized on tunable UHICs, which effectively balanced the kinetic and thermodynamic parameters of crystallization process by fine regulating the CO_2 gas flow rate (Q_{CO_2}) and interfacial correlation factor ($f(r, \theta)$). The combination of kinetic and thermodynamic parameters of crystallization process provided the necessary flexibility to promote the formation of diverse CaCO_3 superstructures.

Based on the classic Hagen Poiseuille transfer model, the mixing and

diffusion efficiency of the developed multi-scale crystallizer can be significantly intensified when the mass transfer scale decreased to the ultra-uniform 200 nm level [49, 50]. Additionally, the proposed interfacial crystallizer was functioning as the aggregation of thousands of parallel microchannels (approximate 6×10^6 channel/ mm^2). It can engineer the biomimetic mineralization procedure by coordinatively regulating the interfacial nucleation and G-L diffusion at the sub-micron pore region, which may shed light on the development of novel flow chemistry and surface chemistry.

4. Conclusion

We proposed a novel interfacial crystallizer with ultra-homo nanoscale through-channel to realize the high selective synthesis of CaCO_3 superstructures during the Gas-Liquid interfacial reactive crystallization. Benefit from the precise control of interfacial structure and superhydrophobic characteristics, the UHIC possessed nanoscale ultra-homo channel and tunable interfacial nuclear energy barrier, ensuring the pre-nucleation cluster of CaCO_3 with sufficient diffusion rate in the sub-micron scale path. High selective synthesis of complex CaCO_3 superstructures was achieved and three kinds of typical crystal morphologies (cubic, polyhedron and sphere) was obtained. Based on the excellent engineering of UHICs, it can effectively realize the function of “interface reactive nucleation-nucleation unit diffusion and growth-high selective synthesis”, which unfold the new path for theoretical research on the non-classic crystal superstructure synthesis. In addition, as a desire interfacial reactive crystallizer, the extensibility and scale-up of UHIC are of great significance for the future development of surface chemistry and material engineering.

Declaration of Competing Interest

The authors declare that they have no known competing financial interests or personal relationships that could have appeared to influence the work reported in this paper.

Acknowledgments

We acknowledge the financial contribution from Science Fund for Creative Research Groups of the National Natural Science Foundation of China (22021005), National Natural Science Foundation of China (Grant No. 21978037), Fundamental Research Funds for the Central Universities (DUT19TD33), and National Key Research and Development Program of China (Grant No. 2019YFE0119200), Support Plan of Innovative Talents of Liaoning Province (XLYC1901005, XLYC1907149), Dalian Innovative Science and Technology Fund (2020JJ26SN064).

Supplementary materials

Supplementary material associated with this article can be found, in the online version, at [doi:10.1016/j.cea.2021.100179](https://doi.org/10.1016/j.cea.2021.100179).

References

- [1] S. Yao, B. Jin, Z. Liu, C. Shao, R. Zhao, X. Wang, R. Tang, Biominerization: from material tactics to biological strategy, *Adv. Mater.* 29 (2017), <https://doi.org/10.1002/adma.201605903>
- [2] A. Dey, G. de With, N.A. Sommerdijk, In situ techniques in biomimetic mineralization studies of calcium carbonate, *Chem. Soc. Rev.* 39 (2010) 397–409, <https://doi.org/10.1039/B811842F>
- [3] G. Zan, Q. Wu, Biomimetic and bioinspired synthesis of nanomaterials/nanostructures, *Adv. Mater.* 28 (2016) 2099–2147, <https://doi.org/10.1002/adma.201503215>
- [4] C. Ruiz-Agudo, J. Lutz, P. Keckelis, M. King, A. Marx, D. Gebauer, Ubiquitin designer proteins as a new additive generation toward controlling crystallization, *J. Am. Chem. Soc.* 141 (2019) 12240–12245, <https://doi.org/10.1021/jacs.9b06473>
- [5] H. Du, E. Amstad, Water: how does it influence the CaCO₃ formation? *Angew. Chem. Int. Ed.* 59 (2020) 1798–1816, <https://doi.org/10.1002/anie.201903662>
- [6] Y. Zhang, J. Wang, C. Wang, Y. Zeng, T. Chen, Crashworthiness of bionic fractal hierarchical structures, *Mater. Des.* 158 (2018) 147–159, <https://doi.org/10.1016/j.matdes.2018.08.028>
- [7] D.V. Volodkin, R. von Klitzing, H. Mohwald, Pure protein microspheres by calcium carbonate templating, *Angew. Chem. Int. Ed.* 49 (2010) 9258–9261, <https://doi.org/10.1002/anie.201005089>
- [8] T. Xiang, J. Hou, H. Xie, X. Liu, T. Gong, S. Zhou, Biomimetic micro/nano structures for biomedical applications, *Nano Today* 35 (2020), 100980, <https://doi.org/10.1016/j.nantod.2020.100980>
- [9] Z. Dong, L. Feng, Y. Hao, M. Chen, M. Gao, Y. Chao, H. Zhao, W. Zhu, J. Liu, C. Liang, Q. Zhang, Z. Liu, Synthesis of hollow biominerallized CaCO₃-polydopamine nanoparticles for multimodal imaging-guided cancer photodynamic therapy with reduced skin photosensitivity, *J. Am. Chem. Soc.* 140 (2018) 2165–2178, <https://doi.org/10.1021/jacs.7b11036>
- [10] A. Fischer, S. Lilenthal, M. Vazquez-Gonzalez, M. Faddeev, Y.S. Sohn, R. Nechushtai, I. Willner, Triggered release of loads from microcapsule-in-microcapsule hydrogel microparticles: en-route to an "artificial pancreas", *J. Am. Chem. Soc.* 142 (2020) 4223–4234, <https://doi.org/10.1021/jacs.9b11847>
- [11] D. Gebauer, S.E. Wolf, Designing solid materials from their solute state: a shift in paradigms toward a holistic approach in functional materials chemistry, *J. Am. Chem. Soc.* 141 (2019) 4490–4504, <https://doi.org/10.1021/jacs.8b13231>
- [12] W.J. Habraken, J. Tao, L.J. Brylka, H. Friedrich, L. Bertinetti, A.S. Schenk, A. Verch, V. Dmitrovic, P.H. Bomans, P.M. Frederik, J. Laven, P. van der Schoot, B. Aichmayer, G. de With, J.J. DeYoreo, N.A. Sommerdijk, Ion-association complexes unite classical and non-classical theories for the biomimetic nucleation of calcium phosphate, *Nat. Commun.* 4 (2013) 1507, <https://doi.org/10.1038/ncomms2490>
- [13] R. Demichelis, P. Raiteri, J.D. Gale, D. Quigley, D. Gebauer, Stable prenucleation mineral clusters are liquid-like ionic polymers, *Nat. Commun.* 2 (2011) 590, <https://doi.org/10.1038/ncomms1604>
- [14] H.C. Rui-Qi Song, An-Wu Xu, Jürgen Hartmann, Markus Antonietti, Polyelectrolyte-directed nanoparticle aggregation: systematic morphogenesis of calcium carbonate by nonclassical crystallization, *ACS Nano* 3 (2009) 1966–1978, <https://doi.org/10.1021/nn900377d>
- [15] L.-B. Mao, L. Xue, D. Gebauer, L. Liu, X.-F. Yu, Y.-Y. Liu, H. Cölfen, S.-H. Yu, Anisotropic nanowire growth via a self-confined amorphous template process: a reconsideration on the role of amorphous calcium carbonate, *Nano. Res.* 9 (2016) 1334–1345, <https://doi.org/10.1007/s12274-016-1029-6>
- [16] G. Di Profio, S.M. Salehi, R. Caliandro, P. Guccione, G. Nico, E. Curcio, E. Fontanarosa, Bioinspired synthesis of CaCO₃ superstructures through a novel hydrogel composite membranes mineralization platform: a comprehensive view, *Adv. Mater.* 28 (2016) 610–616, <https://doi.org/10.1002/adma.201504608>
- [17] W. Zhu, J. Lin, C. Cai, Y. Lu, Biomimetic mineralization of calcium carbonate mediated by a polypeptide-based copolymer, *J. Mater. Chem. B* 1 (2013) 841–849, <https://doi.org/10.1039/C2TB00182A>
- [18] A.F. Wallace, L.O. Hedges, A. Fernandez-Martinez, P. Raiteri, Julian D. Gale, G. A. Waychunas, S. Whitelam, J.F. Banfield, J.J.D. Yoreo, Microscopic evidence for liquid-liquid separation in supersaturated CaCO₃ solutions, *Science* 341 (2013) 885–889, <https://doi.org/10.1126/science.1230915>
- [19] N. Gehrke, H. Co, N. Nassif, Superstructures of calcium carbonate crystals by oriented attachment, *Cryst. Growth Des.* 5 (2005) 2005, <https://doi.org/10.1021/cg050051d>
- [20] R.J.M.N. Jack, J.J.M. Donners, Nico A.J.M. Sommerdijk, A shape-persistent polymeric crystallization template for CaCO₃, *J. Am. Chem. Soc.* 124 (2002) 9700–9701, <https://doi.org/10.1021/ja0267573>
- [21] D. Gebauer, M. Kellermeier, J.D. Gale, L. Bergstrom, H. Colfen, Pre-nucleation clusters as solute precursors in crystallisation, *Chem. Soc. Rev.* 43 (2014) 2348–2371, <https://doi.org/10.1039/C3CS60451A>
- [22] T. Nakamuro, M. Sakakibara, H. Nada, K. Harano, E. Nakamura, Capturing the moment of emergence of crystal nucleus from disorder, *J. Am. Chem. Soc.* 143 (2021) 1763–1767, <https://doi.org/10.1021/jacs.0c12100>
- [23] A.V. Denis Gebauer, Helmut Cölfen, Stable prenucleation calcium carbonate clusters, *Science* 322 (2008) 1819–1822, <https://doi.org/10.1126/science.1164271>
- [24] M. Jehannin, A. Rao, H. Colfen, New horizons of nonclassical crystallization, *J. Am. Chem. Soc.* 141 (2019) 10120–10136, <https://doi.org/10.1021/jacs.9b01883>
- [25] S. Majidi Salehi, A.C. Manjua, B.D. Belviso, C.A.M. Portugal, I.M. Coelhos, V. Mirabelli, E. Fontanarosa, R. Caliandro, J.G. Crespo, E. Curcio, G. Di Profio, Hydrogel composite membranes incorporating iron oxide nanoparticles as topographical designers for controlled heteronucleation of proteins, *Cryst. Growth Des.* 18 (2018) 3317–3327, <https://doi.org/10.1021/cgd.7b01760>
- [26] C.N. Nanev, E. Saridakis, L. Govada, S.C. Kassen, H.V. Solomon, N.E. Chayen, Hydrophobic interface-assisted protein crystallization: theory and experiment, *ACS Appl. Mater. Interfaces* 11 (2019) 12931–12940, <https://doi.org/10.1021/acsm.8b20995>
- [27] S. Yamanaka, N. Ito, K. Akiyama, A. Shimosaka, Y. Shirakawa, J. Hidaka, Heterogeneous nucleation and growth mechanism on hydrophilic and hydrophobic surface, *Adv. Powder Technol.* 23 (2012) 268–272, <https://doi.org/10.1016/j.apt.2012.01.002>
- [28] D.S. Tsekovala, D.R. Williams, J.Y.Y. Heng, Effect of surface chemistry of novel templates on crystallization of proteins, *Chem. Eng. Sci.* 77 (2012) 201–206, <https://doi.org/10.1016/j.ces.2012.01.049>
- [29] S. Luo, X. Kui, E. Xing, X. Wang, G. Xue, C. Schick, W. Hu, E. Zhuravlev, D. Zhou, Interplay between free surface and solid interface nucleation on two-step crystallization of poly(ethylene terephthalate) thin films studied by fast scanning calorimetry, *Macromolecules* 51 (2018) 5209–5218, <https://doi.org/10.1021/acs.macromol.8b00692>
- [30] Q. Wu, A. Gao, F. Tao, P. Yang, Understanding biomolecular crystallization on amyloid-like superhydrophobic biointerface, *Adv. Mater. Interfaces* 5 (2018), 1701065, <https://doi.org/10.1002/admi.201701065>
- [31] A. Koishi, A. Fernandez-Martinez, A.E.S. Van Driessche, L.J. Michot, C.M. Pina, C. Pimentel, B. Lee, G. Montes-Hernandez, Surface wetting controls calcium carbonate crystallization kinetics, *Chem. Mater.* 31 (2019) 3340–3348, <https://doi.org/10.1021/acs.chemmater.9b00417>
- [32] L.P. Yang, X.J. Lin, X. Zhang, W. Zhang, A.M. Cao, L.J. Wan, General synthetic strategy for hollow hybrid microspheres through a progressive inward crystallization process, *J. Am. Chem. Soc.* 138 (2016) 5916–5922, <https://doi.org/10.1021/jacs.6b00773>
- [33] C. Franco, D. Rodriguez-San-Miguel, A. Sorrenti, S. Sevim, R. Pons, A.E. Platero-Prats, M. Pavlovic, I. Szilagyi, M.L. Ruiz Gonzalez, J.M. Gonzalez-Calbet, D. Bochicchio, L. Pesce, G.M. Pavani, I. Imaz, M. Cano-Sarabia, D. Maspoch, S. Pane, A.J. de Mello, F. Zamora, J. Puigmarti-Luis, Biomimetic synthesis of sub-20 nm covalent organic frameworks in water, *J. Am. Chem. Soc.* 142 (2020) 3540–3547, <https://doi.org/10.1021/jacs.9b12389>
- [34] P.-A. Cazade, V. Verma, B.K. Hodnett, D. Thompson, Extended lifetime of molecules adsorbed onto excipients drives nucleation in heterogeneous crystallizations, *Cryst. Growth Des.* 21 (2021) 2101–2112, <https://doi.org/10.1021/cgd.0c01532>
- [35] C. Shahar, S. Dutta, H. Weissman, L.J. Shimon, H. Ott, B. Rybtchinski, Precrystalline aggregates enable control over organic crystallization in solution, *Angew. Chem. Int. Ed.* 55 (2016) 179–182, <https://doi.org/10.1002/ange.201507659>
- [36] D.M.C. Masoud Farhadi-Khouzani, Peng Zhang, Niklas Hedin, Denis Gebauer, Water as the key to proto-aragonite amorphous CaCO₃, *Angew. Chem. Int. Ed.* 55 (2016) 8117–8120, <https://doi.org/10.1002/anie.201603176>
- [37] F. Sebastiani, S.L. Wolf, B. Born, T.Q. Luong, H. Colfen, D. Gebauer, M. Havenith, Water dynamics from THz spectroscopy reveal the locus of a liquid-liquid binodal limit in aqueous CaCO₃ solutions, *Angew. Chem. Int. Ed.* 56 (2017) 490–495, <https://doi.org/10.1002/anie.201610554>
- [38] H. Jiang, J. Zhang, T. Huang, J. Xue, Y. Ren, Z. Guo, H. Wang, L. Yang, Y. Yin, Z. Jiang, M.D. Guiver, Mixed-matrix membranes with covalent triazine framework fillers in polymers of intrinsic microporosity for CO₂ separations, *Ind. Eng. Chem. Res.* 59 (2019) 5296–5306, <https://doi.org/10.1021/acs.iecr.9b04632>
- [39] H. Wang, M. Wang, X. Liang, J. Yuan, H. Yang, S. Wang, Y. Ren, H. Wu, F. Pan, Z. Jiang, Organic molecular sieve membranes for chemical separations, *Chem. Soc. Rev.* (2021), <https://doi.org/10.1039/D0CS01347A>
- [40] X. Zhao, Y. Su, W. Chen, J. Peng, Z. Jiang, Grafting perfluoroalkyl groups onto polyacrylonitrile membrane surface for improved fouling release property, *J. Membr. Sci.* 415–416 (2012) 824–834, <https://doi.org/10.1016/j.membr.2012.05.075>
- [41] P.C. Sahoo, F. Kausar, J.H. Lee, J.I. Han, Facile fabrication of silver nanoparticle embedded CaCO₃ microspheres via microalgae-templated CO₂ biominerallization: application in antimicrobial paint development, *RSC Adv.* 4 (2014) 32562, <https://doi.org/10.1039/C4RA03623A>
- [42] D. Ren, Z. Li, Y. Gao, Q. Feng, Effects of functional groups and soluble matrices in fish otolith on calcium carbonate mineralization, *Biomed. Mater.* 5 (2010), 055009, <https://doi.org/10.1088/1748-6041/5/5/055009>
- [43] J. Chen, X. Zhang, Y. Ge, M. Su, Z. Zhong, The precipitation mechanism of calcium carbonate in the gas-liquid-solid three phase at alkalinity condition, *Cryst. Res. Technol.* 52 (2017), 1600229, <https://doi.org/10.1002/crat.201600229>

- [44] M. Michaud, D. Mangin, C. Charcosset, E. Chabanon, Dense membrane crystallization in gas–liquid systems: key parameters influencing fouling, *Ind. Eng. Chem. Res.* 58 (2019) 20134–20146, <https://doi.org/10.1021/acs.iecr.9b03907>, <https://doi.org/>.
- [45] M. Tian, J. Guo, Z. Wang, J. Cao, X. Gong, Synergetic effect of secondary nucleation and growth on the lithium carbonate particle size in the gas–liquid reactive crystallization of LiCl–NH₃•H₂O–CO₂, *Particuology* 51 (2020) 10–17, <https://doi.org/10.1016/j.partic.2019.10.006>, <https://doi.org/>.
- [46] S. Varma, P.-C. Chen, G. Unnikrishnan, Gas–liquid reactive crystallization for the synthesis of CaCO₃ nanocrystals, *Mater. Chem. Phys.* 126 (2011) 232–236, <https://doi.org/10.1016/j.matchemphys.2010.11.034>, <https://doi.org/>.
- [47] J. Sui, J. Yan, D. Liu, K. Wang, G. Luo, Continuous synthesis of nanocrystals via flow chemistry technology, *Small* 16 (2020), e1902828, <https://doi.org/10.1002/smll.201902828> <https://doi.org/>.
- [48] H. Du, M. Steinacher, C. Borca, T. Huthwelker, A. Murello, F. Stellacci, E. Amstad, Amorphous CaCO₃: influence of the formation time on its degree of hydration and stability, *J. Am. Chem. Soc.* 140 (2018) 14289–14299, <https://doi.org/10.1021/jacs.8b08298>, <https://doi.org/>.
- [49] J. Cai, E. Perfect, C.L. Cheng, X. Hu, Generalized modeling of spontaneous imbibition based on Hagen–Poiseuille flow in tortuous capillaries with variably shaped apertures, *Langmuir: ACS J. Surf. Colloids* 30 (2014) 5142–5151, <https://doi.org/10.1021/la5007204>, <https://doi.org/>.
- [50] L. Falk, J.M. Commenge, Performance comparison of micromixers, *Chem. Eng. Sci.* 65 (2010) 405–411, <https://doi.org/10.1016/j.ces.2009.05.045>, <https://doi.org/>.
- [51] C. Rodriguez-Navarro, C. Jimenez-Lopez, A. Rodriguez-Navarro, M.T. Gonzalez-Muñoz, M. Rodriguez-Gallego, Bacterially mediated mineralization of vaterite, *Geochim. Cosmochim. Acta* 71 (2007) 1197–1213, <https://doi.org/10.1016/j.gca.2006.11.031>, <https://doi.org/>.
- [52] J.M. Walker, B. Marzec, F. Nudelman, Solid-state transformation of amorphous calcium carbonate to aragonite captured by CryoTEM, *Angew. Chem. Int. Ed.* 56 (2017) 11740–11743, <https://doi.org/10.1002/anie.201703158>, <https://doi.org/>.